Structural characterisation of a nanobody derived from a naïve library that neutralises SARS-CoV-2

Jiangdong Huo
Structural Biology, The Rosalind Franklin Institute, Harwell Science & Innovation Campus, OX11 0FA, UK.
Audrey Le Bas
Division of Structural Biology, University of Oxford, The Wellcome Centre for Human Genetics, Headington, Oxford, OX3 7BN, UK.
Reinis R. Ruza
Division of Structural Biology, University of Oxford, The Wellcome Centre for Human Genetics, Headington, Oxford, OX3 7BN, UK.
Helen M.E. Duyvesteyn
Division of Structural Biology, University of Oxford, The Wellcome Centre for Human Genetics, Headington, Oxford, OX3 7BN, UK.
Halina Mikolajek
Diamond Light Source Ltd, Harwell Science & Innovation Campus, Didcot, OX11 0DE, UK.
Tomas Malinauskas
Division of Structural Biology, University of Oxford, The Wellcome Centre for Human Genetics, Headington, Oxford, OX3 7BN, UK.
Tiong Kit Tan
MRC Human Immunology Unit, Weatherall Institute of Molecular Medicine, University of Oxford, John Radcliffe Hospital, Oxford, OX3 9DS, UK.
Pramila Rijal
MRC Human Immunology Unit, Weatherall Institute of Molecular Medicine, University of Oxford, John Radcliffe Hospital, Oxford, OX3 9DS, UK.
Maud Dumoux
Structural Biology, The Rosalind Franklin Institute, Harwell Science & Innovation Campus, OX11 0FA, UK
Philip N. Ward
Division of Structural Biology, University of Oxford, The Wellcome Centre for Human Genetics, Headington, Oxford, OX3 7BN, UK
Jingshan Ren
Division of Structural Biology, University of Oxford, The Wellcome Centre for Human Genetics, Headington, Oxford, OX3 7BN, UK
Daming Zhou
Division of Structural Biology, University of Oxford, The Wellcome Centre for Human Genetics, Headington, Oxford, OX3 7BN, UK

Peter J. Harrison
Division of Structural Biology, University of Oxford, The Wellcome Centre for Human Genetics, Headington, Oxford, OX3 7BN, UK
Julika Radeke
Diamond Light Source Ltd, Harwell Science & Innovation Campus, Didcot, OX11 0DE, UK
Yuguang Zhao
Division of Structural Biology, University of Oxford, The Wellcome Centre for Human Genetics, Headington, Oxford, OX3 7BN, UK
Javier Gilbert-Jaramillo
Sir William Dunn School of Pathology, University of Oxford OX1 3RE, UK
Michael Knight
Sir William Dunn School of Pathology, University of Oxford OX1 3RE, UK
Loic Carrique
Division of Structural Biology, University of Oxford, The Wellcome Centre for Human Genetics, Headington, Oxford, OX3 7BN, UK
Pranav N.M. Shah
Division of Structural Biology, University of Oxford, The Wellcome Centre for Human Genetics, Headington, Oxford, OX3 7BN, UK.
William James
Sir William Dunn School of Pathology, University of Oxford OX1 3RE, UK
Alain Townsend
MRC Human Immunology Unit, Weatherall Institute of Molecular Medicine, University of Oxford, John Radcliffe Hospital, Oxford, OX3 9DS, UK
David I. Stuart
Division of Structural Biology, University of Oxford, The Wellcome Centre for Human Genetics, Headington, Oxford, OX3 7BN, UK
Raymond J. Owens (✉ raymond.owens@rc-harwell.ac.uk)
Structural Biology, The Rosalind Franklin Institute, Harwell Science & Innovation Campus, OX11 0FA, UK
James H. Naismith (✉ naismith@strubi.ox.ac.uk)
Structural Biology, The Rosalind Franklin Institute, Harwell Science & Innovation Campus, OX11 0FA, UK

Research Article

Keywords: SARS-CoV-2, nanobody, H11-D4, spike protein receptor binding domain, human angiotensin-converting enzyme 2

Posted Date: June 1st, 2020

DOI: https://doi.org/10.21203/rs.3.rs-32948/v1

Version of Record: A version of this preprint was published on July 13th, 2020. See the published version at https://doi.org/10.1038/s41594-020-0469-6.

Abstract

The SARS-CoV-2 virus is more transmissible than previous coronaviruses and causes a more serious illness than seasonal flu. The SARS-CoV-2 receptor binding domain (RBD) of the Spike protein binds to the human angiotensin-converting enzyme 2 (ACE2) receptor as a prelude to viral entry into the cell. Using a naïve llama single chain nanobody library and PCR maturation we have produced a nanobody, H11-D4, with a KD 9 nM for RBD that blocks the binding of RBD to the ACE2. Single particle cryo-electron microscopy revealed that H11-D4 binds to each of the three RBDs in the Spike trimer. The 1.8 Å crystal structure of the H11-D4 – RBD complex has illuminated the molecular interactions that drive the high affinity. H11-D4 binds to an epitope on RBD that overlaps with the ACE2 binding, explaining the blocking of ACE2 binding. The nanobody showed potent neutralising activity against live SARS-CoV-2 virus.

Introduction

The SARS-CoV–2 virus is thought, based on sequence identity, to have crossed from bats to humans in 20191. Similar to SARS-CoV (2002–2003) and MERS-CoV (2012), SARS-CoV- 2 presents as a respiratory disease, but can progress into internal organs where it causes organ failure2,3. A recent report from France estimates a fatality rate of 0.7 % and a hospitalisation rate of 3.6%4. Both these rates are much higher in elderly populations4,5. Around 33 % of those admitted to UK hospitals with Covid–19 have died6. Since SARS-CoV–2 also spreads rapidly in the naïve human population7 the current Covid–19 pandemic has presented an unprecedented challenge to modern human society. Although, there is currently no ‘cure’ or vaccine for the disease, passive immune therapy, transfusing critically ill Covid–19 patients with serum from Covid–19 convalescent individuals, has been shown to improve clinical outcomes8,9. This would suggest that neutralisation of the virus, even at a relatively late stage in the disease, may be a useful Covid–19 therapy.

The single positive strand RNA genome of SARS-CoV–2, like SARS-CoV, encodes four major structural proteins; Spike, Envelope, Membrane and Nucleocapsid. The Spike protein comprises an N-terminal (S1) subunit which contains roughly 200 residue receptor binding domain (RBD)10,11 and a C-terminal subunit (S2) which contains the fusion protein12 (Figure 1a). The RBD of SARS-CoV–2 binds more tightly to the extracellular domain of ACE2 (Figure 1a) than the homologous SARS-CoV RBD13. The higher affinity results from sequence changes in RBD (Figure 1b) and this has been proposed to underlie the higher transmissibility of SARS- CoV–214. Antibodies raised to the Spike protein of SARS-CoV can neutralise the virus both *in vitro* and *in vivo* by binding to the RBD and blocking binding to ACE215. Unfortunately, these antibodies do not cross-react with SARS-CoV–2 RBD13. The CR3022 antibody derived from a convalescent SARS-CoV patient is cross-reactive to both SARS-CoV and SARS-CoV–2 RBD (reported apparent KD of 6 nM16). Two studies have reported crystal structures of CR3022 bound to SARS-CoV–2 RBD and show that the target epitope is distant from the ACE2 binding region17,18 consistent with the observation that CR3022 does not block ACE2 binding. One study, has reported highly effective SARS-CoV–2 neutralising activity that appears to arise from destabilisation of the Spike trimer, a novel mechanism18.

Mammalian, including human, antibodies generally have two chains (heavy and light), but camelids in addition to two-chain antibodies also possess a single heavy chain antibody variant19. The antigen-specific variable portion of this single chain antibody is termed the VHH domain and is commonly referred to as a nanobody (Figure 1c). In addition to compatibility with phage display, nanobodies are small, stable and straightforward to produce19. As a result, they serve as alternatives to conventional antibodies as diagnostics, imaging agents and structural biology tools19. The direct application of nanobodies in oncology and inflammatory diseases are being evaluated19,20 with caplacizumab21 approved for use. Nanobodies were developed against SARS-CoV and are currently being developed against SARS-CoV–222 both as research tools and potential therapeutics.

Here we report the identification and characterisation of a high-affinity nanobody (H11-D4) to the Spike protein of SARS-CoV–2 that blocks the attachment of Spike to ACE2 *in vitro.* Structural characterisation of H11-D4 in complex with both full length Spike and the RBD of Spike SARS-CoV–2 has revealed that it targets an epitope immediately adjacent to and slightly overlapping with the ACE2 binding region. H11-D4 is a potent neutraliser of the SARS- CoV–2 infection and therefore may have application on its own or in combination with other antibodies in the treatment of severely ill Covid–19 patients.

Main Text

Identification of a Spike-binding nanobody

Using purified RBD of SARS-CoV–2 as bait, a naïve llama VHH library was screened by *in vitro* phage display technology. The screen identified several nanobodies that bound to the RBD. The tightest binding nanobody, which we denoted H11, had an affinity of < 1 μM (Supplementary Figure 1a, b). Using a random mutagenesis approach, we identified an affinity matured mutant, H11-D4, which differs from H11 at five residues within CDR3 (Figure 1c, 2a). H11-D4 was shown to bind RBD with a KD of 9 nM by SPR (Figure 2b, Supplementary Figure 1c). In a SPR-based competition assay where ACE2-Fc was immobilised and the binding of RBD was monitored in the presence or absence of H11-D4, H11-D4 inhibited the binding of RBD to ACE2 (Figure 2c). This suggested the H11-D4 epitope overlaps with the ACE2 binding site on RBD. When CR3022-Fc was immobilised and the binding of RBD measured, it was found that H11-D4 did not perturb RBD binding (Figure 2d). This indicated that CR3022 and H11-D4 recognised non-overlapping epitopes.

A bivalent Fc-fused construct of H11-D4 competes with ACE2 binding for binding to RBD

H11-D4 was fused to the Fc domain of human IgG1 to produce a homodimeric H11- D4-Fc chimeric protein which is capable of bivalent binding (Figure 3a). The ability of this construct to block ACE2 binding to RBD was tested in two assays. In the first assay, ACE2 was immobilised on plates and the competition between RBD and the analytes (H11-D4-Fc, ACE2- Fc, CR3022-Fc18, VHH72-Fc (a cross-

reactive nanobody from a llama)23) were measured (Figure 3b). This yielded an IC50 of 10 nM for H11-D4-Fc and of 14 nM for VHH72-Fc23. In the second assay, analytes (H11-D4-Fc, ACE2-Fc, CR302218, VHH72-Fc23) and ACE2 were incubated with MDCK cells expressing RBD on their surface (Figure 3c). This assay yielded an IC50 of 99nM for H11-D4-Fc and 96 nM for VHH72-Fc23. As expected, CR3022 shows no binding in either assay since it does not block the RBD—ACE2 interaction17,18.

H11-D4-Fc neutralises virus

The chimeric fusion H11-D4-Fc was tested in plaque reduction neutralisation test for SARS-CoV–2 virus (see Methods). The assay showed 100 % neutralisation at 25 µg/ml and 50 µg/ml. CR3022 was run as a positive control and matches previous reports18. The raw plates are shown in Supplementary Figure 2.

Structural analysis of H11-D4 binding to Spike

H11-D4 was incubated at room temperature for 10 minutes with a purified prefusion- stabilised ectodomain of the SARS-CoV–2 Spike protein (Spike(trimer):H11-D4 mol:mol 1:2). The cryo-EM single particle structure of this variant was recently reported13 and shown to be trimeric with an ‘up - down – down’ arrangement of the three RBDs. The mixture was applied to cryo-EM grids and data collected (see Methods and Supplementary Figure 3a, b, c, d). The maps clearly identified additional density at all three RBDs (Supplementary Figure 3e, f). Improvement in the Coulomb potential maps allowed fitting of the nanobody into the additional density at each RBD (Figure 4a and Supplementary Figure 3f, g, h, i). The density for the nanobody bound to the ‘up’ monomer is weak, but still clearly discernible, whilst the density for the nanobodies bound to the ‘down’ monomers is clearer (Supplementary Figure 3g, h, i).

The region of the RBD in contact with H11-D4 is not well ordered in the EM Spike structures (PDB 6VSB, 6VYB, 6VXX)13,24 and thus it is difficult to ascertain whether the nanobody has altered the local structure of the RBD. The global resolution of the structure (3.4 Å, gold-standard FSC = 0.143) precludes detailed analysis of the interactions that control recognition. The presence of the nanobody has, however, resulted in a 2 Å rigid body shift in the ‘up’ domain relative to the non-complexed form13,24 (Supplementary Figure 4a). The movement of the ‘up’ RBD is required to avoid a clash between it and a separate nanobody that is bound to neighbouring ‘down’ RBD (Supplementary Figure 4a).

Nanobodies rely on three variable loops denoted CDR1, CDR2 and CDR3 to form the antigen-binding site (Figure 1c). To gain insight into the molecular basis of recognition, a 1.8 Å resolution structure of the complex between H11-D4 and SARS-CoV–2 RBD was determined (see Methods and Figure 4b). In the H11-D4—RBD complex, CDR1 contributes very little to the interface (Figure 4c). In CDR2, residues Arg52, Ser54 and Ser57 are in contact with RBD (Figure 4c). From CDR3, Glu100 to Leu106 make contacts with RBD (Figure 4c). The surface on RBD which contacts H11-D4 is formed by Lys444 to Phe456 and Gly482 to Ser494 (Figure 4d). These two stretches of RBD sequence comprise over 90 % of buried surface area

and make all the hydrogen bonds with H11-D4 (Figure 4e). Notably the aromatic ring of Tyr449 in RBD stacks against a hydrophobic patch on H11-D4 at Asn101 (Supplementary Figure 5a).

We noted the key role of Arg 52 from CDR2 of H11-D4, it sits at the heart of a network of interactions, including RBD residues Glu 484 (bivalent salt link) and Phe 490 (the aromatic ring π-stacks with the guanidine group) (Figure 4e). Arg 52 seems also to play a role in stabilising the conformation of the CDR3 loop of H11 as it forms hydrogen bonds to the backbone carbonyls of Arg 103, Ser 104 and side chain of Tyr 109 (Figure 4f). The seven- residue stretch of H11-D4 CDR3 region, which varied during maturation, contributes over 60% of the surface area buried by the complex and makes five hydrogen bonds to RBD (Figure 4e). All the contacts between the two proteins are shown in Figure 4e.

Arg 98 is the only maturation change in the CDR3 loop that does not contact RBD (Supplementary Figure 5b). Rather, this residue salt bridges to Glu 100 and makes hydrogen bonds to several residues in CDR1, suggesting it is important for ordering the CDR3 and CDR1 loops. Trp 112 of H11-D4 adopts two conformations both of which stack against the Arg 103- Asp 108 salt bridge (Supplementary Figure 5c), an interaction that also appears important to the structure of the CDR3 region.

Using the H11-D4 - RBD complex, we created a model of three nanobodies bound to ‘down’ (closed) form of the Spike24 (Supplementary Figure 4b). This model does not disclose any clashes, suggesting the nanobody would bind to the Spike protein in all its conformational states (Supplementary Figure 4b).

Superposition of the RBD - ACE2 complex10 reveals that H11-D4 would, consistent with biophysics (Figure 2c), plate assays (Figure 3b, c) and neutralisation experiments (Figure 3d), prevent ACE2 binding to RBD (Figure 5a). This is due to van der Waals clashes, principally between regions of H11-D4 that are not in contact with the RBD and regions of ACE2 (also not in contact with RBD) (Figure 5a). Interestingly the contact surface of H11-D4 on RBD shows only a small overlap with the ACE2 contact surface (Figure 1b, Figure 5b). Comparison with the RBD—ACE2 complex10,11 reveals that binding of H11-D4 results in a hinging movement of RBD residues 439–506 (Supplementary Figure 5d). There are local changes in a turn that is centred at Val483 of the RBD that occur upon binding H11-D4 (Supplementary Figure 5e)

Given the potential for synergistic effects that can arise from combinations of antibodies / nanobodies that recognise different epitopes, we obtained diffracting crystals of the ternary complex consisting of H11-D4, RBD and CR3022 in two crystal forms each with two copies of the asymmetric unit (space groups, *P4122* 3.3 Å and *P21212* 2.7 Å). In *P4122* one copy was less well ordered, whilst in the *P21212* crystal form both copies were equally ordered. The nanobody and antibody bind to non-overlapping epitopes (Figure 5c) consistent with biophysical analysis (Figure 2d). The epitope on RBD recognised by CR3022 has previously been described17,18 and the binding of H11-D4 has not altered this interaction. When compared to RBD—CR3022 complex, the presence of the H11-D4 has resulted in a hinging motion within the RBD (Supplementary Figure 5f) similar to that already noted. The interactions between H11-D4 and RBD not affected by CR3022. Superimposing the two copies of the RBD molecule found in the *P21212* reveals that two molecules of H11-D4 are offset by 6°, superimposing the H11-D4 - RBD complex reveal it sits between these two “extremes” (Supplementary Figure 5g).

Discussion

It is assumed that during the virus life cycle the Spike trimer exists in an equilibrium between the all ‘down’ configuration and mixed ‘up down’ states13. The Spike protein can only bind to ACE2 with the RBD in the ‘up’ state11 and this results in dissociation of the trimer. SARS-CoV–2 Spike binds to ACE2 with a 10 to 20-fold higher affinity (KD of ~15 nM) than SARS- CoV Spike, a fact that has been proposed to drive its higher transmissibility13,25. Neutralising antibodies that have been identified to date for SARS-CoV bind to the RBD of the Spike protein and most (except CR3022 which operates by a novel mechanism18) do so by blocking ACE2 binding26. We have shown that H11-D4 binds with high affinity to RBD (Figure 2b), blocks ACE2 binding (Figures 2c, 2d, 3b, 3c) and neutralises the virus (Figure 3d).

Structural analysis suggests that H11-D4 would be able to bind to all known conformations of RBD within the Spike (Figure 4a and Supplementary Figure 4b). The ability of the smaller nanobody to access epitopes inaccessible to conventional antibodies is well known and several nanobodies are in clinical trials19 with Caplacizumab21 now approved for use. The epitope on SAR-CoV–2 RBD that is recognised by H11-D4 overlaps only to a limited degree with the ACE2 binding region (Figure 5a, b). This region of SARS-CoV–2 RBD shows a number of sequence changes when compared to SARS-CoV RBD (Figure 1b). The Pro469– Pro470 turn in the SARS-CoV RBD structure27 is very different to the structure at Val 483 Glu 484 in SARS-CoV–2. Additional sequence and structural changes (SARS-CoV - SARS-CoV–2) at Tyr 442—Leu 455, Trp 476—Phe 490, Asn 479—Gln 493 combine to present a very different epitope and would seem to preclude cross-reactivity of H11-D4. The lack of conservation of the H11-D4 epitope between SARS-CoV and SARS-CoV–2 raises the possibility SARS-CoV–2 variants may emerge that retain ACE2 receptor binding but are no longer recognised by H11- D4 or its relatives. At least some of the plausible escape mutations would perturb the position of Phe 486 which inserts into a cleft in ACE2, an interaction important to SARS-CoV–2’s increased affinity28. The rapid pipeline from naïve library screen to maturation and thorough characterisation does offer the possibility that new nanobodies could be generated against SARS-CoV–2 viruses that have escaped H11-D4.

The characterisation of the cross-reactive (SARS-CoV KD 7 nM and SARS-CoV–2 KD 40nM) nanobody VHH72 has been reported recently23. This nanobody blocks ACE2 binding and shows neutralisation activity (IC50 0.2 µg/mL) against the SARS-CoV–2 pseudovirus23. Crystal structures of complexes between VHH72 and the RBD from MERS-CoV and SARS-CoV23 show that VHH72 recognises an epitope that is different from that bound by H11-D4 (Supplementary Figure 6a). Interestingly, the epitope bound by VHH72 partly overlaps with the epitope bound by CR302218 (Supplementary Figure 6b). This suggests naïve library based methods may identify different epitopes than immune systems perhaps due to different selection pressures. Another antibody, which like CR3022 does not block ACE2 binding but neutralises the virus has also been published29 but there are no further structural details. Humanised nanobodies with potent neutralisation activity against SARS-CoV–2 virus (most potent IC50 0.2- 0.5 µg/ml in Vero cells) have been described30. Some, but not all, of these nanobodies blocked ACE2 binding and no molecular insights into their mode of action were reported30.

The use of convalescent serum has shown clinical promise in patients severely ill with SARS-CoV31 and most recently SARS-CoV–29; such passive immune therapy has a long history in medicine32. The use of laboratory produced reagents avoids some of the infection risks that arise from use of human serum and can be administered in smaller volumes. The direct injection of a nanobody has shown promise in a mouse model of cobra venom intoxication33. Camelid VHH domains are highly conserved with human counter parts and their immunogenicity has been proposed to be low34 although humanisation strategies are well developed35.

To increase *in vivo* half-life and enhance avidity, nanobodies can be dimerised by a variety of means20. For our *in vitro* binding assays (Figure 3b, c) and neutralisation experiments (Figure 3d) we created a dimeric Fc fusion construct (Figure 3a). This construct showed potent neutralisation activity against live virus. The previously reported neutralising CR3022 antibody17,18 or VHH7223 both recognise a different epitope than H11-D4 (Figure 2d, 5c), and may be candidates for synergistic combination with H11-D4 in passive immunisation therapy.

This work establishes that nanobody maturation technology can be deployed to produce high affinity bind agents against an emerging viral threat in real time. The approach may be useful in identifying complementary epitopes to those identified by animal immunisation approaches. The H11-D4 nanobody may find application in a cocktail of lab synthesised neutralising antibodies given for passive immunisation of severely ill Covid–19 patients.

Methods

Protein production

All primers used in this work are listed in Supplementary Table 1

The gene encoding amino acids 1-1208 of the SARS-CoV-2 spike glycoprotein ectodomain, with mutations of RRAR > GSAS at residues 682-685 (the furin cleavage site) and KV > PP at residues 986-987, as well as inclusion of a T4 fibritin trimerization domain, an HRV 3C cleavage site, a 8xHis tag and a Twin-Strep-tag at the C-terminus13 was synthesised and subcloned into a pHLsec vector between the AgeI and XhoI restriction sites37. The validity of the clone was confirmed by sequencing.

The SARS-CoV-2 spike receptor binding domain (RBD) T332-K529 with Pro 527 omitted was generated by PCR with a template of full length COVID-19 spike synthetic construct (gift from Sarah Gilbert, Oxford Jenner Institute). The primers used were RBD_T332_F and RBD_T332_R. The PCR product was cut with AgeI-KpnI and cloned into a lenti-viral transfer vector pHR-CMV-TetO238. The lentivirus was generated by co-transfection of the above transfer vector with a packaging (psPAX2) and an envelope plasmid (pMD2.G) into HEK293T Lenti-X cells as described38. The virus containing supernatant was used to transduce HEK293S(GNTI-) cells 39. The cells were expanded and grown in roller bottles in DMEM (high glucose, Sigma) with 10 % FBS (Invitrogen) for 3 days and changed to 2 % FBS DMEM media for a week before harvesting. The conditioned media were buffer exchanged with PBS, the N- terminal His-tagged

RBD was captured with a 5 ml HisTrap nickel column (GE Healthcare), eluted with 300 mM imidazole in PBS and further polished with a Superdex 75 HiLoad 16/600 gel filtration column (GE Healthcare) with running buffer of 10 mM Hepes, pH 7.4, 150 mM NaCl. For crystallisation with CR3022, H11-D4 and RBD were deglycosylated with Endoglycosidase F1. CR3022-Fc production has been described previously18. HEK293T cells were transfected with two plasmids encoding the heavy and light chains of Fab CR3022 and purified as above.

The sequence of VHH72 was obtained from Wrapp et al23. The codon optimised gene with Fc-fusion tag synthesized by GeneArt was cloned into the Abvec-Heavy vector (Genbank FJ475055) between restriction sites AgeI and HindIII. The protein was expressed using Expi293F cells according to the manufacturer's protocol, affinity purified using Protein A MabSelect SuRE column (GE Healthcare) and buffer-exchanged to PBS.

CR3022-Fc was constructed with the resident human Cκ and IgG1 CH1 sequences and a signal sequence. Synthetic genes encoding the constant regions were inserted by Infusion® cloning into PmeI-HindIII cut pOPING-ET40. The vectors have been engineered so that VL and VH sequences can be inserted into the KpnI- BsiWI (pOPINhuVL) and KpnI-SfoI (pOPINhuVH) restriction sites by Infusion® cloning. Synthetic genes encoding the candidate variable regions of CR302241 were purchased from IDT Technologies as gBlocks. The VH gene was amplified using the forward primer CR3022_VH_F and the reverse primer CR3022_VH_R; the VL gene was amplified using the forward primer CR3022_VL_F and the reverse primer CR3022_VL_R. The genes were inserted into the pOPIN expression vectors by Infusion® cloning.

The CR3022 hIgG1 heavy chain gene of the CR3022-Fc construct was amplified through joining three fragments A-C (fragment A: using the forward primer CR3022_Full_F and the reverse primer CR3022_TVSS_R, with CR3022 VH as template; fragment B: using the forward primer CR3022_TVSS_F and the reverse primer CR3022_linker_R, with CR3022 VH as template; fragment C: using the forward primer CR3022_linker_F and the reverse primer CH3_R, with pOPINTTGneoFc as template) using the forward primer CR3022_Full_F and the reverse primer CH3_R. The gene was inserted into the vector42 incorporating a C-terminal His6 tag.

The gene encoding amino acids 330-532 of RBD of SARS-CoV-2 (Gene ID: MN908947) was amplified from a synthetic gene (IDT Technologies) using the forward primer RBD_F and the reverse primer RBD_His_R or the reverse primer RBD_BAP_R and inserted into the vector pOPINTTGneo incorporating either a C-terminal His6 or BirA-His6 tag. The gene was also amplified using the forward primer RBD_F and the reverse primer RBD_Fc_R and inserted into the vector pOPINTTGneoFc incorporating a C-terminal hIgG1Fc-His6 tag. SARS-CoV-2 RBD mutants were generated by site-directed mutagenesis using primers listed in Supplementary Table 1, amplified using the forward primer RBD_F and the reverse primer RBD_BAP_R, and inserted into the vector pOPINTTGneo to incorporate a BirA-His6 tag. The gene encoding amino acids 317-518 of the RBD of SARS-CoV-1 (Gene ID: NC_004718.3) was purchased from IDT Technologies as "Infusion-ready" gBlocks and inserted into the vector pOPINTTGneo-BAP incorporating a BirA-His6 tag.

The gene encoding amino acids 19-615 of the human ACE2 was amplified from an image clone (Sourcebiosciences, clone ID: 5297380) using the forward primer ACE2_F and the reverse primer ACE2_R and inserted into pOPINTTGneo incorporating a C-terminal His6. The gene was also amplified using the forward primer ACE2_F and the reverse primer ACE2_Fc_R and inserted into the vector pOPINTTGneoFc incorporating a C-terminal hIgG1Fc-His6 tag.

The gene encoding amino acids 1-1208 of the SARS-CoV-2 spike glycoprotein ectodomain, with mutations of RRAR > GSAS at residues 682-685 (the furin cleavage site) and KV > PP at residues 986-987, as well as inclusion of a T4 fibritin trimerisation domain, a HRV 3C cleavage site, a His-6 tag and a Twin-Strep-tag at the C-terminus, as reported by Wrapp *et al*13.

All vectors were sequenced to confirm clones were correct. Recombinant RBDs, RBD mutants, RBD-Fc, ACE2, ACE2-Fc, CR3022 Fab and CR3022-Fc were transiently expressed in Expi293™ (Thermo Fisher Scientific); SARS-CoV-2 RBD used for crystallisation was expressed in the presence of 1 µg/mL Kifunensine. Proteins were purified from culture supernatants by an immobilised metal affinity using an automated protocol implemented on an ÄKTAxpress (GE Healthcare, UK), followed by a Hiload 16/60 Superdex 75 or a Superdex 200 10/300GL column, using phosphate-buffered saline (PBS) pH 7.4 buffer. Recombinant Spike ectodomain was expressed by transient transfection in HEK293S GnTI- cells (ATCC CRL-3022) for 9 days at 30 °C. Conditioned media was dialysed against 2x phosphate buffered saline pH 7.4 buffer. The Spike ectodomain was purified by immobilised metal affinity chromatography using Talon resin (Takara Bio) charged with cobalt followed by size exclusion chromatography using HiLoad 16/60 Superdex 200 column in 20 mM Tris pH 8.0, 150 mM NaCl, 10 mM HEPES pH 8.0, 0.02 % NaN3 at 4 °C.

VHH library screening

A VHH phage display library (Abcore Inc. Ramona, CA, USA) constructed in the vector pADL- 20c and comprising approximately 1 x 1010 independent clones was inoculated into 2xTYA (2xTY supplemented with 100 µg/mL ampicillin) and infected with M13 helper phage to obtain a library of VHH-presenting phages. Phages displaying VHHs specific for the SARS-CoV-2 RBD were enriched after two rounds of bio-panning on 50 nM and 5 nM of RBD, respectively, through capturing with Dynabeads™ M-280 (Thermo Fisher Scientific). For each round of panning the Dynabeads and phages were firstly blocked with StartingBlock™ (PBS) Blocking Buffer (Thermo Fisher Scientific) for 30 minutes; the phages were incubated with the RBD for 1 hour, and then 5 minutes with the Dynabeads (Thermo Fisher Scientific); and subsequently washed 6 times with PBS supplemented with 0.05 % Tween 20 and 1 time with PBS. The retained phages were eluted through incubation with TBSC buffer (10 mM Tris pH 7.4, 137 mM NaCl, 1 mM CaCl2) and 1 mg/mL trypsin (Sigma-Aldrich) for 30 min. The collected phages were amplified in exponentially growing TG1 *E. coli* cells and plated on 2xTY agar plates supplemented with 100 µg/mL ampicillin. Enrichment after each round of panning was determined by plating the cell culture with 10-fold serial dilutions. After the second round of panning, 93 individual clones were picked to inoculate 2xTYA and were grown overnight, shaking at 250 rpm and 37 0C. The next day, the overnight culture was used to inoculate 2xTYA and infected with M13 helper phage to obtain clonal VHH-presenting phages.

Enzyme-linked immunosorbent assays

The wells of microtiter plates (Greiner high and medium binding) were coated with 5 µg/mL neutravidin in PBS pH 7.4 overnight at 4 oC. The next day, the wells were coated with 50 nM biotinylated RBD, and then blocked with 3 % milk powder in PBS pH 7.4. Supernatant of clonal phage was added into each well, binding was detected by incubating the wells with HRP- Conjugated anti-M13 (GE Healthcare). After washing, 100 µL of TMB substrate (SeraCare) was added and absorbance at 405 nM was measured with a Microplate Absorbance Reader.

Affinity maturation of nanobody H11

Mutations in the CDR3 of nanobody H11 were introduced by PCR using seven pairs of forward and reverse primers forward primers in Supplementary Table 1 (H11_AM_CDR3_F1-7 in combination with H11_AM_CDR3_R1-7). The mutated fragments were amplified with the primers H11_Phd_F and H11_Phd_R, digested with SfiI restriction enzyme and cloned into pADL-23c phagemid (Antibody Design Laboratories, San Diego CA, USA). The ligated vector was transformed into TG1 cells by electroporation to give a phage library consisting approximately 2 × 109 independent clones. Two rounds of bio-panning of the library were carried out on 5 nM and 1 nM of RBD, respectively, as described above and positive phage was identified by ELISA and sequencing.

Production of nanobodies

For initial biophysical screening of the nanobodies, the phagemid was transformed into the WK6 *E. coli* strain and grown in TB medium (supplemented with 100 µg/mL ampicillin and 1 mM MgCl2), shaking at 225 rpm and 37 oC, with induction of protein expression by 1 mM IPTG at OD ~ 1.2, and then grown overnight, shaking at 225 rpm and 20 oC. The bacterial cells were pelleted and re-suspended in PBS, and processed by a cell disruptor (Constant Systems) according to manufacturer's instructions. The supernatant was harvested through centrifugation at 33733 x *g* and subsequently filtered through a 0.8 µm filter. The His-tagged nanobodies were purified from the whole-cell lysate by immobilised metal affinity column then followed by a Superdex 75 10/300GL column, using PBS pH 7.4 buffer.

For final biophysical characterisation of the nanobodies, the genes of nanobody were amplified using a pair of primers OmA_exp_F and OmA_exp_R and cloned into the vector pOPINO. The plasmid was transformed into the WK6 *E. coli* strain and grown in TB medium (supplemented with 100 µg/mL ampicillin and 1 mM MgCl2), shaking at 180 rpm and 37 oC, with induction of protein expression by 1 mM IPTG at OD ~ 1.2, and then grown overnight, shaking at 180 rpm and 28 oC. The bacterial cells were pelleted and re-suspended in TES buffer (0.2 M Tris pH 8, 0.5 mM EDTA, 0.5 M sucrose) overnight at 4 oC, followed by 2 hours in TES/4 buffer (TES diluted 4x in water). The supernatant was harvested through centrifugation at 9715 x *g* and subsequently filtered through a 0.8 µm filter. The His-tagged nanobodies were purified from the periplasmic extract by using Ni-NTA agarose resin (Agarose Bead Technologies) according to the manufacturer's instructions, followed by size-exclusion chromatography with a Hiload 16/60 Superdex 75 column, using PBS pH 7.4 buffer.

To generate Fc fusion of the nanobodies, the sequences were amplified with the forward primer H11-Fc_F and the reverse primer H11-Fc_R, inserted into pOPINTTG-3C-Fc and protein purified as described above.

Surface plasmon resonance

The surface plasmon resonance experiments were performed using a Biacore T200 (GE Healthcare). All assays were performed using a Sensor Chip Protein A (GE Healthcare), with a running buffer of PBS pH 7.4 supplemented with 0.005 % v/v Surfactant P20 (GE Healthcare) at 25 °C.

To determine the binding affinity of nanobody H11 for the SARS-CoV-2 RBD, RBD-Fc was immobilized onto the sample flow cell of the sensor chip. The reference flow cell was left blank. Nanobody H11 was injected over the two flow cells at a range of 8 concentrations prepared by serial two-fold dilutions from 2.5 μM, at a flow rate of 30 μL/min, with an association time of 60 s and a dissociation time of 60 s. The data were fitted to a 1:1 binding model and to calculate KD using GraphPad Prism 8.

To determine the binding kinetics between the SARS-CoV-2 RBD and nanobody H11- D4, RBD-Fc was immobilized onto the sample flow cell of the sensor chip. The reference flow cell was left blank. Nanobody H11-D4 was injected over the two flow cells at a range of five concentrations prepared by serial two-fold dilutions from 50 nM, at a flow rate of 30 μL/min using a single-cycle kinetics program with an association time of 60 s and a dissociation time of 60 s. Running buffer was also injected using the same program for background subtraction. All data were fitted to a 1:1 binding model using the Biacore T200 Evaluation Software 3.1.

To determine the cross-reactivity of nanobody H11-D4 against the SARS-CoV-2 RBD mutants, H11-D4-Fc was immobilised onto the sample flow cell of the sensor chip. The reference flow cell was left blank. A single injection of SARS-CoV-2 RBD mutants with a concentration of 200 nM was performed with an association time of 60 s and a dissociation time of 60 s. All data were fitted to a 1:1 binding model using the Biacore T200 Evaluation Software 3.1.

To determine the binding of SARS-CoV-1 RBD for nanobody H11-D4 and ACE2, H11- D4-Fc or ACE2-Fc was immobilized onto the sample flow cell of the sensor chip. The reference flow cell was left blank. A single injection of SARS-CoV-2 RBD mutants with a concentration of 1 μM was performed with an association time of 60 s and a dissociation time of 360 s.

In the competition assay where CR3022-Fc or ACE2-Fc was used as the ligand, approximately 1000 RU of CR3022-Fc or ACE2-Fc was immobilised. The following samples were injected: (1) a mixture of 1 μM nanobody H11-D4 and 0.1 μM RBD; (2) a mixture of 1 μM E08R (anti-Caspr2 Fab) Fab and 0.1 μM RBD; (3) 0.1 μM RBD; (4) 1 μM nanobody H11-D4; (5) 1 μM E08R Fab. All injections were performed with an association time of 60s and a dissociation time of 600s. All curves were plotted using GraphPad Prism 8.

ACE2 blocking and neutralisation experiments

ACE2-Fc (amino acids 18-615) was expressed in Expi293F cells (Thermo Fisher Scientific) and purified using a Histrap HP column (GE Healthcare). 2 mg/mL of ACE2-Fc in PBS was applied to NUNC plates (Immunosorp, Thermo Fisher Scientific) overnight at 4 OC, washed 4 times with PBS and blocked in 5 % skimmed milk for 2 hours at RT prior to the assays. RBD-6H (amino acid 340-538; NITN .. GPKK) was chemically biotinylated using EZ-link Sulfo-NHS-Biotin (A39256; Life Technologies). Biotinylated RBD and analyte (in 20-fold molar excess over biotinylated RBD) diluted in PBS/0.1 % BSA (in duplicates) were mixed and transferred to the coated NUNC plates for 1 hour. A second layer Streptavidin-HRP (P0397, Dako) diluted 1:600 in PBS/0.1 % BSA was then added. Plates were then washed with PBS 4 times and signal was developed by adding POD substrate (11484281001, Roche) for 5 min before stopping with 1 M H2SO4. Plates were read at OD450 on a Clariostar plate reader. The control analyte (a non- blocking anti influenza N1 antibody) was used to obtain maximum signal and PBS only wells were used to determine background. Graphs were plotted as % binding of biotinylated RBD to ACE2. Binding % = (X - Min)/(Max - Min)*100 where X = Measurement of the competing component, Min = Buffer without binder biotinylated RBD-6H, Max = Biotinylated RBD-6H alone. Inhibitory concentration at 50% (IC50) of the nanobodies against ACE2 was determined using non-linear regression [inhibitor] versus normalised response curve fit using GraphPad Prism 8.

MDCK-SIAT1 cells were stably transfected with RBD (amino acids 340-538 NITN.GPKK). RBD expressing cells were FACS sorted using the CR3022 antibody. Cells (3 x 104 per well) were seeded the day before the assay. ACE2-Fc was biotinylated as above. A serial half log dilution (ranging 1 mM to 0.1 nM) of analytes and controls were performed in a U-bottomed 96 well plate in 30 mL volume. PBS supplemented with 0.1 % BSA (37525; Thermo Fisher Scientific) was used for dilution of all components. 30 mL of biotinylated Ace2-Fc at 10 nM was added to titrated analytes. Cells were washed with PBS and 50 mL of each mixture of ACE2 and an analyte was transferred to the cells and incubated for 1 h at room temperature. Cells were then washed with PBS and incubated for 1 h with the second layer Streptavidin-HRP (P0397, Dako) diluted to 1:800 and developed as above. Graphs were plotted as % binding of biotinylated ACE2 to RBD. Binding % = (X - Min)/(Max - Min)*100 where X = Measurement of the competing component, Min = Buffer without binder biotinylated ACE2-Fc, Max = Biotinylated ACE2-Fc alone. Inhibitory concentration at 50 % (IC50) of the nanobodies against ACE2 was determined using non-linear regression [inhibitor] versus normalised response curve fit using GraphPad Prism 8. Non-biotinylated ACE2-Fc-6H and VHH72-Fc were used as positive controls.

Plaque reduction neutralization tests were performed using passage 4 of SARS-CoV-2 Victoria/01/2020 using established methodology43. In brief, virus suspension at appropriate concentrations in Dulbecco's Modification of Eagle's Medium containing 1 % FBS (D1; 100 mL) was mixed with nanobody-Fc (100 mL) diluted in D1 at a final concentration of 50 mg/mL, 25 mg/mL, 12.5 ug/mL or 6.125 mg/mL, in triplicate, in wells of a 24 well tissue culture plate, and incubated at room temperature for 30 minutes. Thereafter, 0.5 mL of a single cell suspension of Vero E6 cells in D1 at 5 x 105/mL was added, and incubated for 2 h at 37 °C before being overlain with 0.5 mL of D1 supplemented with carboxymethyl cellulose (1.5 %). Cultures were incubated for a further 4 days at 37 °C before plaques were revealed by staining the cell monolayers with amido black in acetic acid/methanol (Supplementary Figure 2).

H11-D4 complex with Spike, preparation and Cryo-EM Data Collection

Both purified spike protein and H11-D4 nanobody were separately buffer exchanged into 20 mM Tris (pH 8.0), 200 mM NaCl, 0.02 % NaN_3 buffer using a desalting column (Zeba, Thermo Fisher Scientific) just before complex preparation. The Spike protein at a final concentration of 0.2 mg/mL was incubated with the H11-D4 at a 1:6 molar ratio at room temperature for 10 minutes. 3 µL of the resulting sample was then applied to a holey carbon- coated 200 mesh copper grid (C-Flat, CF-2/1, Protochips) that had been freshly glow- discharged on high for 20 s (Plasma Cleaner PDC-002-CE, Harrick Plasma). Excess liquid was removed by blotting for 6 s with a blotting force of -1 using vitrobot filter paper (grade 595, Ted Pella Inc.) at 4.5 °C, 100 % relative humidity. Blotted grids were then immediately plunge- frozen using a Vitrobot Mark IV (Thermo Fisher Scientific).

Frozen grids were first screened on a Glacios microscope operating at 200 kV (Thermo Fisher Scientific) before imaging on a Titan Krios G2 (Thermo Fisher Scientific) at 300 kV. Movies (40 frames each) were collected in compressed tiff format on a K3 detector (Gatan) in super resolution counting mode using a custom EPU version 2.5 (Thermo Fisher Scientific) with a defocus range of 0.8-2.6 µm and at a nominal magnification of x105,000, corresponding to a calibrated pixel size of 0.83 Å/pixel, see Supplementary Table 2.

Motion correction and alignment of 2x binned super-resolution movies was performed using Relion (v3.1)44 with a 5 x 5 patch based alignment. CTF-estimation of full- frame non-weighted micrographs was performed using GCTF (v1.06) and non-template- driven particle picking was then performed within cryoSPARC (v2.14.1-live)45 followed by multiple rounds of 2D classification. The resulting 2D class averages consistent with Spike trimer were used for template-driven particle picking before further rounds of 2D and 3D classification with C1 symmetry. The resulting map from the most populous class was then sharpened in cryoSPARC before conversion to Relion-format star files using custom pyEM scripts46 (csparc2star.py, https://github.com/asarnow/pyem) for further CTF refinement within Relion.

Data processing and refinement statistics are given in Supplementary Table 2. An initial model for Spike was generated using PDB ID, 6VXX24 and rigid body fitted into the map using Chimera47 followed by Coot48. For the nanobody-bound RBD, the crystal structure reported here was superimposed onto the naked Spike model in Coot and checked for fit in the density. S1/S2 domains split into subdomains for each subunit (residues 27-307; 308-321 and 591-700 ; 322-333 and 529-590; 701-1147) were then independently rigid body fitted in Coot48. before a final real space refinement with PHENIX49 with hydrogen atoms added using ReadySet49resulting in a final correlation coefficient of 0.8. The H11-D4 - RBD crystal structure was used as reference structure restraints during refinement of the Spike owing to the density. Rounds of manual inspection in Coot48 and real space refinement with PHENIX49 resulted in the final model. Data and refinement statistics are shown in Supplementary Table 2.

H11-D4 - RBD - CR3022 ternary complex crystallography

Purified RBD, Fab CR3022 and nanobody H11-D4 were mixed together at a molar ratio of 1:1:1 to a final concentration of approximately 7 mg/mL and incubated at room temperature for one hour. Initial screening was performed in 96-well plates using the nanolitre sitting-drop vapour diffusion method. The best crystals were grown in condition containing 0.1 M sodium citrate tribasic dihydrate, pH 5.0, 10 % (w/v) Polyethylene glycol 6000.

Crystals were soaked in cryoprotectant containing 75 % reservoir solution and 25 % glycerol for a few seconds, then mounted in loops and frozen in liquid nitrogen prior to data collection at beamline I03 of Diamond Light Source, UK. Diffraction images were recorded on an Eiger2 XE 16M detector with exposure time of 0.008 s per frame, beam size 50×20 µm and 100 % beam transmission. Data were indexed, integrated and scaled with the automated data processing program Xia2-dials50,51.

Diffraction data from 3 crystals, 360° each, were merged to give a final data set to 3.3 Å resolution with 78-fold redundancy. The crystal structure of RBD - CR3022 complex (PDB ID, 6YLA18) and the structure of nanobody 9G8 (PDB ID, 4KRP52) that has 79 % sequence identity and same CDR3 length with H11-D4 were used for molecular replacement search with PHASER53. There are two H11-D4 - RBD - CR3022 ternary complexes in the crystal asymmetric unit, resulting in a crystal solvent content of ~69 %.

Model rebuilding was done with COOT48, initially refined with PHENIX49 then with REFMAC554 aided by PDB-REDO55, MOLPROBITY56 and the TLSMD server57. One of the H11- D4 molecules which has well defined electron density, allowed the model rebuilding. However, the second H11-D4 molecule that is located in a large solvent tunnel and has little contact within the crystal lattice has a poorly defined electron density. Statistics for X-ray data collection and structure refinement are given in Supplementary Table 3.

H11-D4 - RBD complex crystallography

The gene of nanobody H11-D4 was amplified using a pair of primers OmA_exp_F and OmA_exp_R and cloned into the vector pOPINO. The plasmid encoding for H11-D4 was transformed into WK6 Su- cells and the cells were grown in 5 L of terrific broth to an OD of 1.2. The protein expression was induced with 1 mM IPTG overnight at 28 °C. The cells were harvested 15 min at 5000 x *g*. The pellet was resuspended in 105 mL of TES buffer (0.2 mM Tris pH 8.0, 0.5 mM EDTA and 0.5 M sucrose) under agitation overnight at 4°C (30 mL/L culture). A further 210 mL of TES was added along with 25 mg/mL of DNase I for 2h. The samples were then centrifuged for 30 min at 9820 x *g*, 4 °C. The supernatant was filtered using 0.45 µm filter and then purified on an AKTA Express (GE Healthcare) with a 5 mL Ni-NTA column (GE Healthcare), pre-equilibrated in 50 mM NaPi pH 7, 1 M NaCl, 30 mM imidazole. The protein was eluted in 50 mM NaPi pH 7, 150 mM NaCl, 300 mM imidazole, and injected on gel filtration Superdex S75 16/600 (GE Healthcare) in the buffer 50 mM Tris pH 7, 150 mM NaCl. The protein fractions were pooled and concentrated using a 5 kDa MWCO concentrator to 12 mg/mL.

The nanobody H11-D4 was then mixed with 8.7 mg of RBD at 2.9 mg/mL at a molar ratio H11-D4:RBD 1.1:1 and the complex was incubated for 3 h in a cold room under agitation at 2 rpm. RBD-H11D4 was

then deglycosylated by adding 0.4 mg of EndoH glycosidase and incubated overnight at room temperature, under agitation at 2 rpm. The mixture was then concentrated to 1 mL with a 5 kDa MWCO concentrator and injected on gel filtration using a Superdex 200 10/300 (GE) in 50 mM Tris pH 7, 150 mM NaCl. The peak fractions were pooled and concentrated using 5 kDa MWCO concentrator to 10 mg/mL, 18 mg/mL and 29 mg/mL.

Crystallization screenings on the H11-D4 - RBD complex were performed on the Diamond/RCaH/RFI HTP crystallization facility at Harwell. Crystals were grown at 20 °C using the sitting drop vapor diffusion method by mixing 0.2 mL of the 18 mg/mL H11-D4 RBD complex with 0.1 mL of the crystallization buffer containing 0.2 M Sodium acetate trihydrate, 0.1 M MES pH 6.0, 20 % w/v PEG 8000. The crystals grew overnight and were flash cooled in a solution containing the mother liquor with 30 % (v/v) ethylene glycol. Diffraction data were also collected and processed at beamline I03 at Diamond Light Source as describe above. The structure was solved by molecular replacement53 using the RBD and H11-D4 monomers from the ternary complex above. Refinement was carried out as described above for the ternary complex. Statistics for X-ray data collection and structure refinement are given in Extended Date Table 3.

Declarations

Acknowledgments

This work was supported by the Rosalind Franklin Institute, funding delivery partner EPSRC. PPUK is funded by the Rosalind Franklin Institute EPSRC Grant no. EP/S025243/1. J.H.N., A.LB., P.W. are supported by Wellcome Trust (100209/Z/12/Z). X-ray data used Diamond Light Source COVID-19 Rapid Access time on Beamline I03, experiment MX27031-1.

T.M. is supported by Cancer Research UK grants C20724/A14414 and C20724/A26752 to Christian Siebold. JGJ is funded by National Secretariat of Education (Senescyt – IFTH, Ecuador). HMED is supported by Wellcome. J.R. is supported by the Wellcome Trust (101122/Z/13/Z), D.I.S. by the UK Medical Research Council (MR/N00065X/1) . D.I.S., P.R. and

A.T. are funded by the Chinese Academy of Medical Sciences (CAMS) Innovation Fund for Medical Science (CIFMS), China (grant number: 2018-I2M-2-002). The core virus neutralisation facility is supported by gifts to the Oxford Covid19 Research Response Fund.

Competing interests

The authors declare no competing interests.

Corresponding authors

Raymond J Owens (raymond.owens@rc-harwell.ac.uk) and James H Naismith (naismith@strubi.ox.ac.uk)

Data availability

The coordinates and structure factors of the ternary SARS-CoV-2 H11-D4 – RBD – CR3022 complex (6YZ7, 6Z2M) and the binary SARS-CoV-2 H11-D4 - RBD complex (6YZ5). EM maps are deposited in EMDB with accession codes 6Z43 for the prefusion Spike with H11-D4. The data that support the findings of this study are available from the corresponding authors on request.

References

1. Menachery, V. D. et al. A SARS-like cluster of circulating bat coronaviruses shows potential for human emergence. Nat Med 21, 1508-1513 (2015).
2. Ronco, C., Reis, T. & Husain-Syed, F. Management of acute kidney injury in patients with COVID-19. The Lancet Respiratory Medicine 1-5 (2020).
3. Jaiswal, N. K. & Saxena, S. K. in Medical Virology: From Pathogenesis to Disease Control: Coronavirus Disease 2019 (COVID-19) 141-150 (Springer Singapore, Singapore, 2020).
4. Salje, H. et al. Estimating the burden of SARS-CoV-2 in France. Science (2020).
5. Adams, M. L., Katz, D. L. & Grandpre, J. Population-Based Estimates of Chronic Conditions Affecting Risk for Complications from Coronavirus Disease, United States. Emerg Infect Dis 26, (2020).
6. Docherty, B. et al. Features of 16,749 hospitalised UK patients with COVID-19 using the ISARIC WHO Clinical Characterisation Protocol. (2020).
7. Kucharski, A. J. et al. Early dynamics of transmission and control of COVID-19: a mathematical modelling study. Lancet Infect Dis (2020).
8. Bloch, E. M. et al. Deployment of convalescent plasma for the prevention and treatment of COVID-19. J Clin Invest (2020).
9. Shen, C. et al. Treatment of 5 Critically Ill Patients With COVID-19 With Convalescent Plasma. JAMA (2020).
10. Wan, Y., Shang, J., Graham, R., Baric, R. S. & Li, F. Receptor Recognition by the Novel Coronavirus from Wuhan: an Analysis Based on Decade-Long Structural Studies of SARS Coronavirus. J Virol 94, (2020).
11. Yan, R. et al. Structural basis for the recognition of SARS-CoV-2 by full-length human ACE2. Science 367, 1444-1448 (2020).
12. Li, F. Structure, Function, and Evolution of Coronavirus Spike Proteins. Annu Rev Virol 3, 237-261 (2016).
13. Wrapp, D. et al. Cryo-EM structure of the 2019-nCoV spike in the prefusion conformation. Science 367, 1260-1263 (2020).
14. Hoffmann, M. et al. SARS-CoV-2 Cell Entry Depends on ACE2 and TMPRSS2 and Is Blocked by a Clinically Proven Protease Inhibitor. Cell 181, 271-280.e8 (2020).

15. Zhu, Z. et al. Potent cross-reactive neutralization of SARS coronavirus isolates by human monoclonal antibodies. Proc Natl Acad Sci U S A 104, 12123-12128 (2007).
16. Tian, X. et al. Potent binding of 2019 novel coronavirus spike protein by a SARS coronavirus-specific human monoclonal antibody. Emerg Microbes Infect 9, 382-385 (2020).
17. Yuan, M. et al. A highly conserved cryptic epitope in the receptor-binding domains of SARS-CoV-2 and SARS-CoV. Science (2020).
18. Huo, et al. Neutralization of SARS-CoV-2 by destruction of the prefusion Spike. OI:10.1101/2020.05.05.079202 (2020).
19. Jovčevska, I. & Muyldermans, S. The Therapeutic Potential of Nanobodies. BioDrugs 34, 11-26 (2020).
20. Chanier, T. & Chames, P. Nanobody Engineering: Toward Next Generation Immunotherapies and Immunoimaging of Cancer. Antibodies (Basel) 8, (2019).
21. Peyvandi, F. et al. Caplacizumab reduces the frequency of major thromboembolic events, exacerbations and death in patients with acquired thrombotic thrombocytopenic purpura. J Thromb Haemost 15, 1448-1452 (2017).
22. Zhou, P. et al. A pneumonia outbreak associated with a new coronavirus of probable bat origin. Nature 579, 270-273 (2020).
23. Wrapp, D. et al. Structural Basis for Potent Neutralization of Betacoronaviruses by Single-domain Camelid Antibodies. Cell (2020).
24. Walls, A. C. et al. Structure, Function, and Antigenicity of the SARS-CoV-2 Spike Glycoprotein. Cell 181, 281-292.e6 (2020).
25. Song, W., Gui, M., Wang, X. & Xiang, Y. Cryo-EM structure of the SARS coronavirus spike glycoprotein in complex with its host cell receptor ACE2. PLoS Pathog 14, e1007236 (2018).
26. Suits, M. D., Sperandeo, P., Dehò, G., Polissi, A. & Jia, Z. Novel structure of the conserved gram-negative lipopolysaccharide transport protein A and mutagenesis analysis. J Mol Biol 380, 476-488 (2008).
27. Li, , Li, W., Farzan, M. & Harrison, S. C. Structure of SARS coronavirus spike receptor- binding domain complexed with receptor. Science 309, 1864-1868 (2005).
28. Shang, J. et al. Structural basis of receptor recognition by SARS-CoV-2. Nature (2020).
29. Wang, et al. A human monoclonal 1 antibody blocking SARS-CoV-2 infection. Nature Communications 11, 2251 (2020).
30. Chi, et al. Humanized Single Domain Antibodies Neutralize SARS-CoV-2 by Targeting Spike Receptor Binding Domain. bioRxiv (2020).
31. Mair-Jenkins, J. et al. The effectiveness of convalescent plasma and hyperimmune immunoglobulin for the treatment of severe acute respiratory infections of viral etiology: a systematic review and exploratory meta-analysis. J Infect Dis 211, 80-90 (2015).
32. Slifka, M. K. & Amanna, I. J. Passive immunization. Plotkin's Vaccines, 7th Edition 8, 84-95 (2018).

33. Richard, G. et al. In vivo neutralization of α-cobratoxin with high-affinity llama single- domain antibodies (VHHs) and a VHH-Fc antibody. PLoS One 8, e69495 (2013).
34. Klarenbeek, A. et al. Camelid Ig V genes reveal significant human homology not seen in therapeutic target genes, providing for a powerful therapeutic antibody platform. MAbs 7, 693-706 (2015).
35. Vincke, C. et al. General strategy to humanize a camelid single-domain antibody and identification of a universal humanized nanobody scaffold. J Biol Chem 284, 3273-3284 (2009).
36. Laskowski, R. A. & Swindells, M. B. LigPlot+: multiple ligand-protein interaction diagrams for drug discovery. J Chem Inf Model 51, 2778-2786 (2011).

Figures

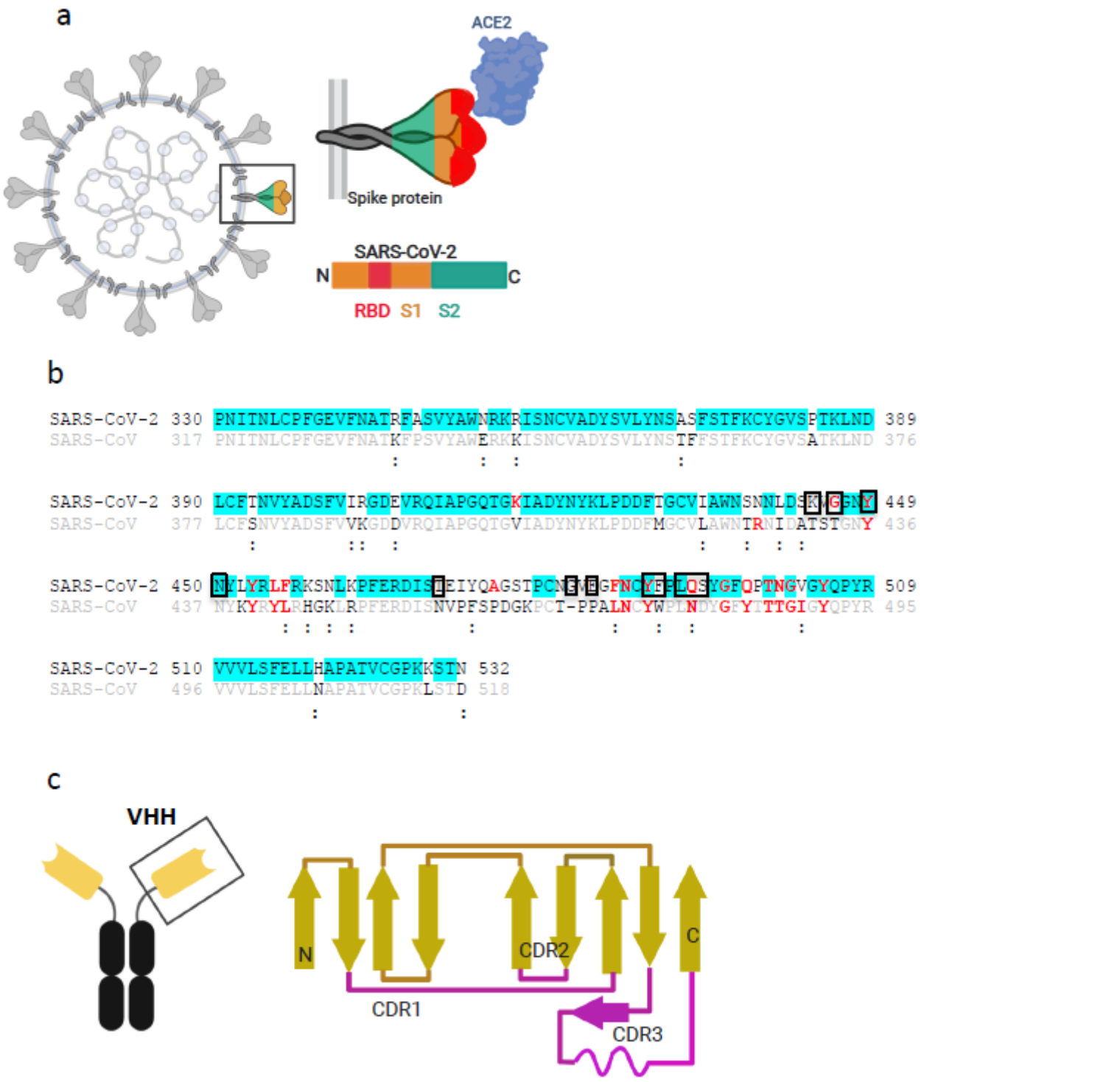

Figure 1

The Spike protein of SARS-CoV-2 drives infection. (a) Schematic representation of the Spike protein of SARS-CoV-2. The Spike protein is composed of the S1 and S2 subunits. The S1 domain contains the receptor binding domain (RBD) which is highlighted in red. Using the RBD, the trimeric Spike molecule binds to ACE2 on human cells (a single ACE2 is shown in blue). (b) Residues of the RBD which are shared between SARS-CoV-2 and SARS-CoV are highlighted in cyan (SARS-CoV-2) and shown in light grey text

(SARS-CoV). Residues which contact ACE2 are highlighted in red for each sequence. Sequence differences in SARS-CoV are in black text, conservative substitutions are denoted by colons (:) below. Residues in contact with H11-D4 nanobody are boxed. (c) Camelids have antibodies that are dimers of a single chain, the constant region is in black and the variable region is in yellow. When the VHH domain is expressed on its own, it is termed a nanobody. A topology diagram shows the nanobody is composed of two β-sheets. Three loops CDR1, CDR2 and CDR3 control antigen binding and are highlighted in purple.

a

H11	97 A QTRVTRS LLSDYATWPYDY 116
H11-D4	A **RTENVR**S LLSDYATWPYDY

b

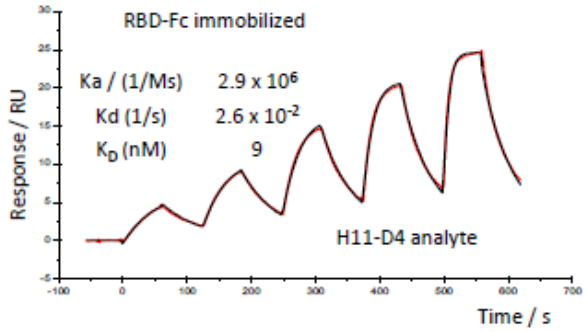

c

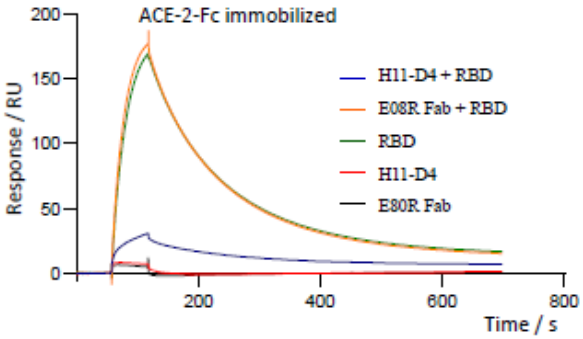

d

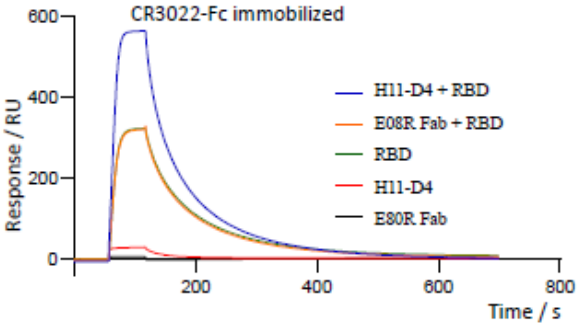

Figure 2

High affinity nanobodies to Spike protein. (a) Maturation by mutagenesis of CDR3 region of H11 results in tighter binding. Changes from the parent are shown in bold. The changes all occur in a seven-residue stretch. (b) A sensorgram shows that the H11-D4-Fc fusion binds to an RBD immobilised on a chip with 9 nM affinity. A repeat is included in Supplementary Figure 1. (c) H11-D4 competes with RBD for binding to an immobilised ACE2 molecule, indicating H11- D4 could block viral engagement with ACE2. The antibody E08R (anti-Caspr2 Fab) is a negative control that is not expected to bind. (d) Both H11-D4 and RBD bind to the immobilised CR3022 antibody, suggesting CR3022 and H11-D4 recognise different epitopes.

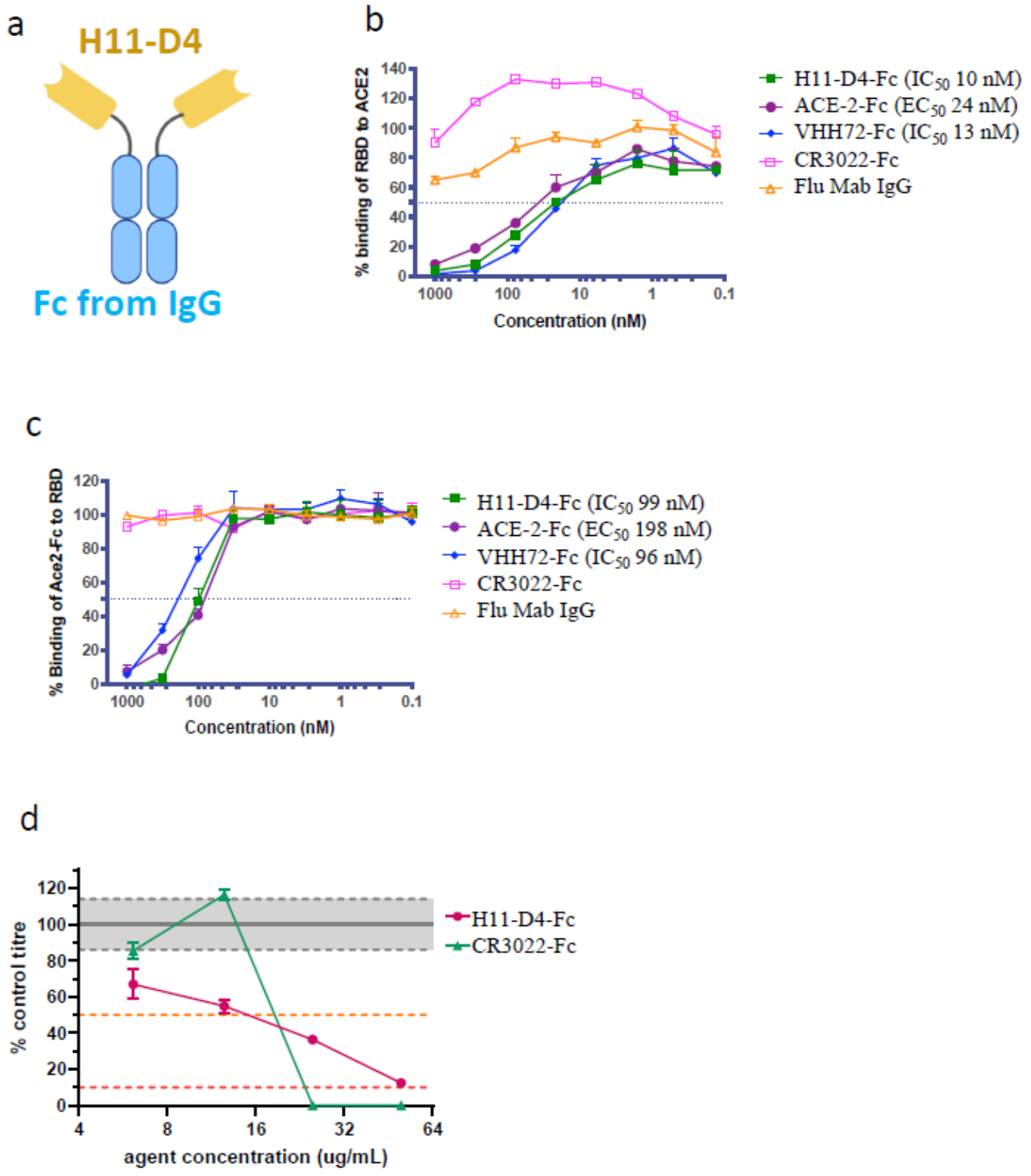

Figure 3

In vitro activity of high affinity nanobodies. (a) Schematic representation of the IgG1 Fc (blue) fused with nanobody (yellow) construct that was constructed for in vitro assays. (b) Biotinylated RBD was mixed with analytes at various ratio and then added to plates coated with ACE2-Fc. The amount of biotin label that bound to the plate was measured. Experiments were performed in triplicate with the mean +/- SD are shown. EC50 is calculated by linear interpolation and IC50 calculated as described in Methods. (c)

Analytes at various concentrations were mixed with biotin labelled ACE2-Fc (1 µg/ml) and added to MDCK-SIAT1 cells expressing RBD on the cell surface. The amount of biotinylated ACE-2 bound to the cell was measured. Experiments were performed in triplicate with the mean +/- SD are shown. Analysis was carried out as described in Methods. (d) H11-D4-Fc at 25 µg/ mL shows 100 % neutralisation of live wild type virus in a Vero cell- based assay. Experimental plates are shown in Supplementary Figure 2.

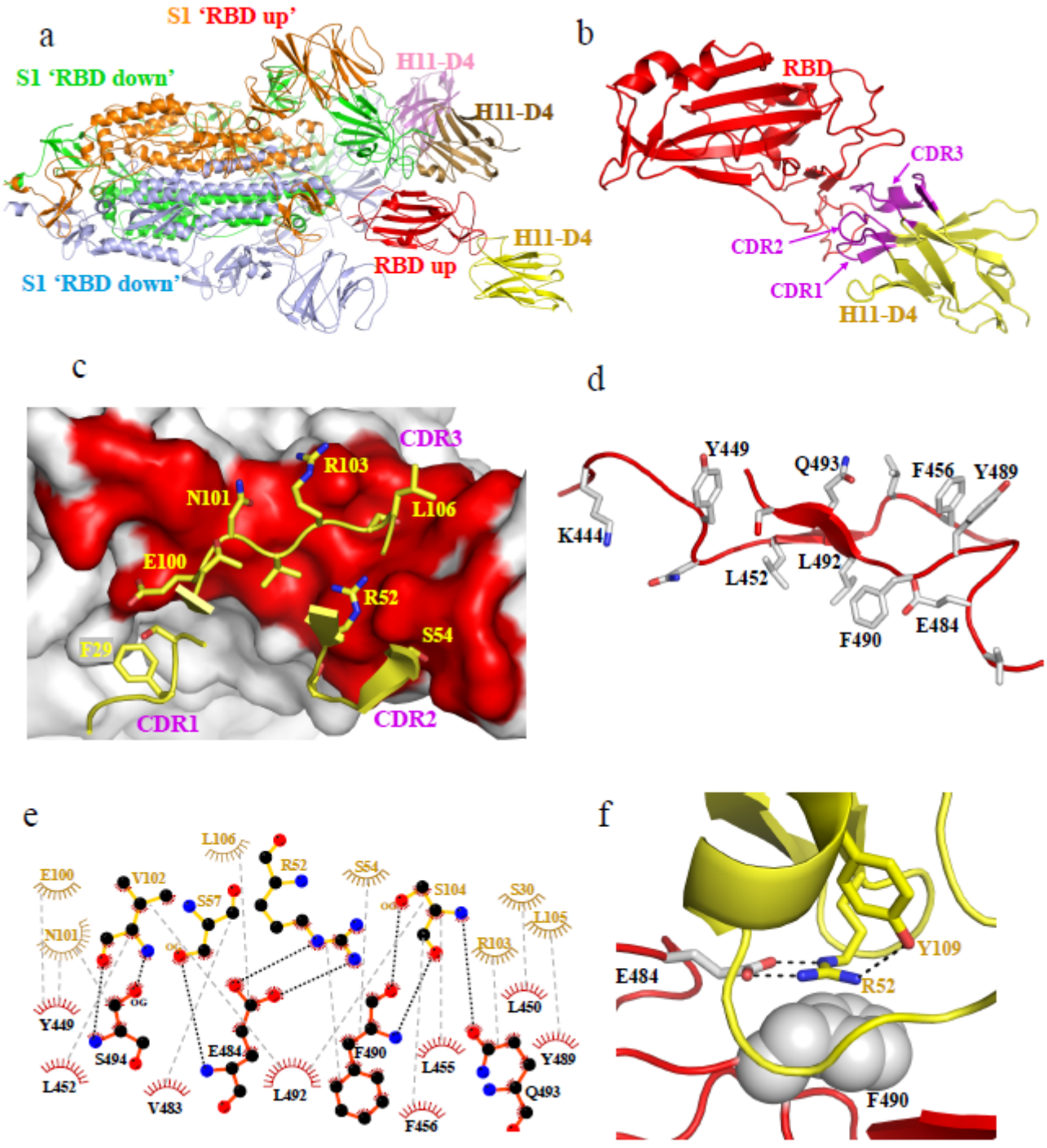

Figure 4

Structure of H11-D4 nanobody bound to the RBD domain. (a) EM structure of Spike (S1) trimer with each of three chains bound to one H11-D4 nanobody. The 'up' configured monomer of the Spike is coloured

orange with its RBD highlighted in red. The H11-D4 nanobody bound to the ‘up’ RBD is coloured dark yellow. One of the ‘RBD down’ chains of the Spike is coloured pale blue throughout and the nanobody bound to its RBD is coloured pale pink; the other ‘RBD down’ chain is coloured green with its bound nanobody coloured pale brown. (b) The crystal structure of the H11-D4 (dark yellow) and RBD (red) complex. The loops CDR1, CDR2 and CDR3 which control the recognition and are highlighted in magenta. (c) A 90° rotation of the structure shown in Figure 4b, showing the residues in contact with RBD. H11-D4 residues are labelled in yellow with carbon atoms coloured yellow, nitrogen atoms blue and oxygen atoms red. RBD is shown as a surface with contact points (4.0 Å) in red. (d) The same view as in Fig. 4c, showing the RBD residues in contact with H11-D4. Selected RBD residues are labelled in black, with carbons coloured in grey other atoms are coloured as H11-D4. (e) LigPlot36 detailing the interaction between H11-D4 (residues shown in dark yellow) and RBD (residues shown in red). Arg 27 which is not well ordered in the crystal structure was not included in this analysis. The hydrogen bonds are shown in black and van der Waals interactions in light grey. (f) Arg52 of CDR2 of H11-D4 stacks against Phe 490 of RBD and makes salt contacts with Glu 484. H11-D4 residues are coloured as Figure 4c. RBD residues are labelled in black, with carbons coloured in grey other atoms are coloured as H11-D4.

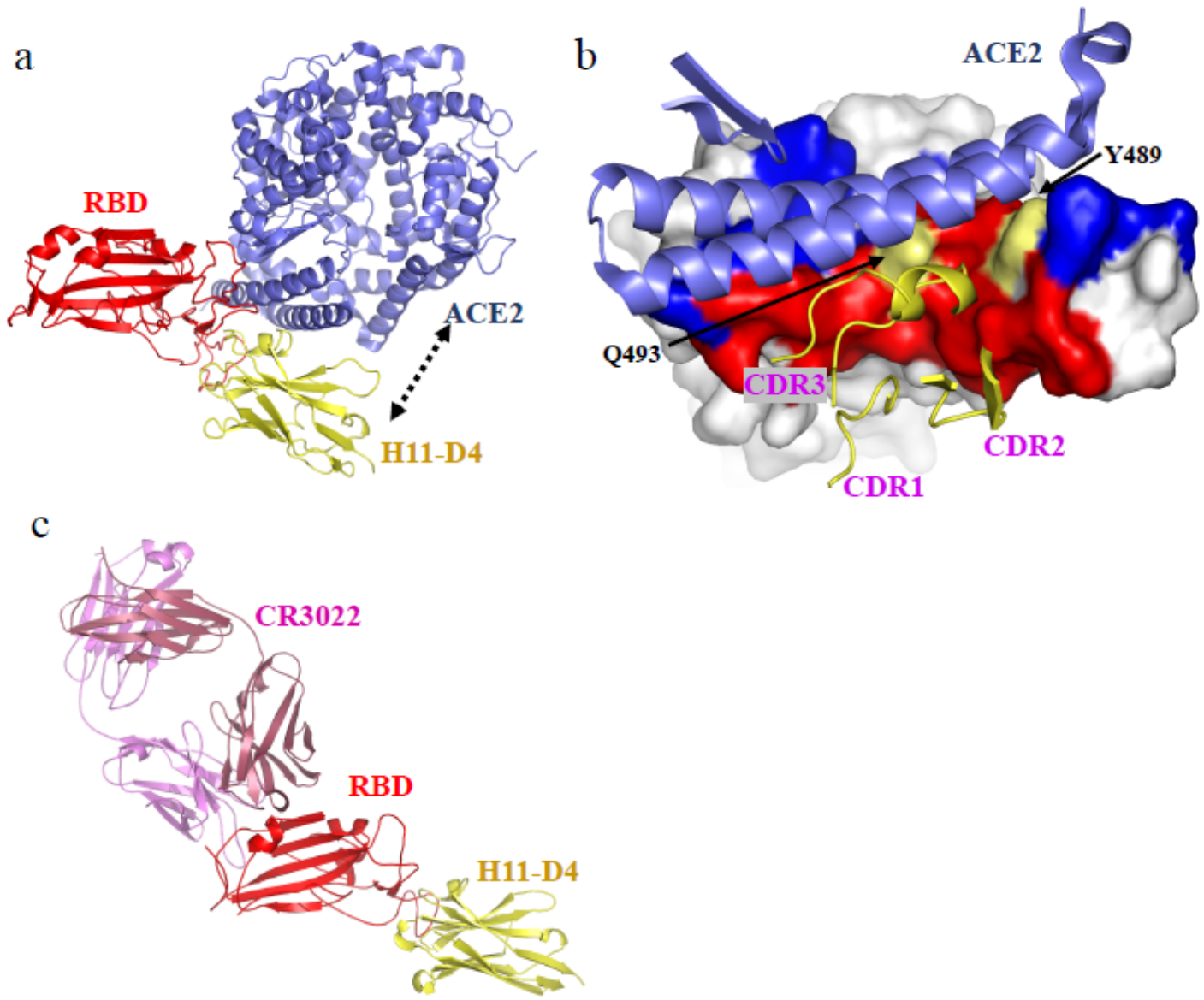

Figure 5

RBD has different binding epitopes for H11-D4 and CR3022. (a) Superposition of the H11-D4 – RBD complex (coloured as Figure 4b) with the RBD – ACE2 complex10 (ACE2 coloured in pale blue) shows that when H11-D4 is bound to RBD it would prevent ACE2 binding to RBD by steric clashes. (b) The region of RBD that engages ACE2 only has a small overlap with that region recognised by H11-D4. The RBD is shown as a molecular surface, those regions that only contact ACE2 are highlighted in dark blue, whilst those that only contact H11-D4 are in red. The two helices and turn of ACE2 that contact RBD are shown in cartoon and coloured as Figure 5a. CDR1, 2 and 3 of H11-D4 are labelled, shown in cartoon and coloured in dark yellow. The two residues Tyr 489 and Gln 493 that contribute significantly to both binding sites are highlighted in pale yellow. (c) The ternary complex H11-D4 (yellow), RBD (red) and CR3022 (pale pink and lilac), shows the nanobody and antibody recognise entirely different epitopes.

Supplementary Files

This is a list of supplementary files associated with this preprint. Click to download.

- Supplementarytablesandfigures.pdf